DE GRUYTER Z. Phys. Chem. 2024; 238(11): 2075–2100

Halil Arslan*, Alexei Kuzmin, Ilze Aulika, Dmitrii Moldarev, Max Wolff,
Daniel Primetzhofer, Inga Pudza, Karlis Kundzins,
Anatolijs Sarakovskis, Juris Purans and Smagul Zh Karazhanov

Chemical state and atomic structure in stoichiovariants photochromic oxidized yttrium hydride thin films

https://doi.org/10.1515/zpch-2023-0507
Received December 4, 2023; accepted January 19, 2024; published online February 28, 2024

Abstract: We investigate the effective oxidation state and local environment of yttrium in photochromic YHO thin film structures produced by e-beam evaporation, along with their chemical structure and optical properties. Transmission electron microscopy images reveal the oxidized yttrium hydride thin film sample exhibiting a three-layered structure. X-ray photoelectron spectroscopy (XPS) measurements manifest that the oxidation state of yttrium is modified, dependent on the film's composition/depth. Furthermore, Ion beam analysis confirms that this variability is associated with a composition gradient within the film. X-ray absorption spectroscopy at the Y K-edge reveals that the effective oxidation state of yttrium is approximately +2.5 in the transparent/bleached state of YHO. Spectroscopic ellipsometry investigations showed a complex non-linear optical depth profile of the related sample confirming the dominant phase of YHO and the presence of Y_2O_3 and Y towards the middle of the film. The first evidence of (n; k) dispersion curves for e-beam sputtered photochromic YHO thin films are reported for transparent and dark states.

Keywords: mixed anion materials; oxidized yttrium hydride; electronic structure; chemical bonding; e-beam evaporated photochromic thin films; depth-resolved analyses

---

***Corresponding author: Halil Arslan**, Institute of Solid State Physics, University of Latvia, Kengaraga Street 8, LV-1063 Riga, Latvia, E-mail: halil@cfi.lu.lv. https://orcid.org/0000-0002-9383-384X
Alexei Kuzmin, Ilze Aulika, Inga Pudza, Karlis Kundzins, Anatolijs Sarakovskis and Juris Purans, Institute of Solid State Physics, University of Latvia, Kengaraga Street 8, LV-1063 Riga, Latvia
Dmitrii Moldarev, Max Wolff and Daniel Primetzhofer, Department of Physics and Astronomy, The Ångström Laboratory, Uppsala University, P.O. Box 516, SE-75120 Uppsala, Sweden
Smagul Zh Karazhanov, Institute of Solid State Physics, University of Latvia, Kengaraga Street 8, LV-1063 Riga, Latvia; and Institute for Energy Technology, P.O. Box 40, NO-2027 Kjeller, Norway

1 Introduction

Yttrium oxyhydride (YHO) exhibits photochromic properties under ambient conditions [1], making it of interest for applications in building windows and attracting increasing research attention. So far, the material has been obtained in the form of thin films through various methods, including magnetron sputtering [1–6], electron beam evaporation [7, 8], as well as in powder form synthesized through chemical processes [9, 10] and magnetron sputtering [11]. It is worth noting that the material's properties are significantly influenced by the deposition method, film composition, and microstructure. For example, YHO films produced via magnetron sputtering or electron beam evaporation on glass substrates exhibit high resistivity [1] whereas the epitaxial films deposited on yttria-stabilized zirconia (111) and CaF_2 (111) substrates by magnetron sputtering can demonstrate lower resistivity [6]. Sputter-deposited powder exhibit photochromic properties, while YHO powder obtained through chemical methods do not [9, 11]. Furthermore, the photochromic performance of YHO films deposited by magnetron sputtering [12, 13] surpasses that of films produced through electron beam evaporation [7, 8].

Compared to YHO films deposited using magnetron sputtering, there has been limited research on the photochromic performance of films produced through electron beam evaporation. Currently, critical information remains scarce, with limited knowledge accessible, which includes the establishment of a relationship between the composition of YHO films and their photochromic performance [7]. *In-situ* growth and characterization have been conducted by continuously monitoring changes in mass during deposition, oxidation, and illumination, as well as by examining the chemical composition and depth profiles [8].

The existing literature points to two primary approaches for understanding the kinetics that govern the transition between transparent and colored (dark) states in photochromic materials (YHO). The first approach involves scrutinizing the structural and chemical changes, with the utmost significance lying in the fact that these alterations occur within a single phase. In 2020, a study conducted by Baba et al. provided an understanding of the light-induced reversible structural transformation (lattice expansion and contraction) in photochromic YHO, integrating experimental findings with theoretical insights [12].

In contrast, the second method emphasizes studying anion transfer, specifically highlighting the interaction between multi/dual phases. In 2020, Hans et al., published a paper describing the photochromic gadolinium oxyhydride and its dual-phase (Gd_2O_3, and GdH_2) formation. In their study, they proposed photon-induced hydrogen transfer between these two phases. This intriguing phenomenon led the authors to conclude that the photochromism in gadolinium/yttrium oxyhydride results from the dynamic interaction and exchange of hydrogen atoms between the REM_2O_3, and $REMH_2$ phases (REM: Gd, Y) [14].

Furthermore, important findings from previous research [15] have revealed that the photochromism of Y(D,H)O films is not connected to long-distance material transport. There is no evidence of light-induced or thermal diffusion of hydrogen over extended distances, yet deuteride thin films exhibit a strong and robust photochromic response. Nevertheless, it is crucial to emphasize that the underlying mechanism responsible for this behavior remains elusive.

Today, the most extensively studied photochromic YHO films are those deposited using magnetron sputtering, with promising prospects for commercialization in the coming years. Yttrium oxyhydride has undergone a comprehensive investigation employing advanced characterization techniques. For instance, extended X-ray absorption spectroscopy fine structure (EXAFS) has been utilized to unveil the intricate atomic-scale structural arrangement of oxygen atoms surrounding yttrium atoms [2, 16]. In a different study, the assessment of the Y, O, and H local environments, coupled with an analysis of the oxidation states of anions in YHO thin films and powders, was conducted by combining NMR studies with DFT calculations [17]. Furthermore, instrumental techniques such as X-ray photoelectron spectroscopy (XPS) [12], ion beam analysis (IBA) [5], and spectroscopic ellipsometry (SE) [13] have been employed in these studies to investigate the elemental composition, determine the chemical state of the cation, and assess its optical properties.

Although magnetron sputtering is a scalable method commonly employed in the glass industry for large-area depositions, offering uniform film coverage, it tends to exhibit slower deposition rates when reactive sputtering is utilized. Additionally, it consumes more electrical energy, particularly due to the requirement for sustaining a plasma. Therefore, the exploration of material properties through more cost-effective and user-friendly methods, such as electron beam evaporation, holds significant importance.

The primary objective of this study is to extensively investigate the properties of photochromic YHO thin films. This investigation entails ascertaining the effective oxidation state of Y and scrutinizing the local cationic environment within the films when they are in their bleached state. Furthermore, we aim to delve into potential chemical interactions among the ternary elements Y, O, and H. To achieve these objectives, we harnessed advanced characterization techniques, including XPS, XAS, Transmission Electron Microscopy (TEM), and IBA. The YHO powder we produced, renowned for its good photochromic properties and well-documented structure in our earlier study [11], was used as a reference material for the primary characterization techniques, including XRD and XAS, in this study.

Unlike previous publications, this paper is dedicated to conducting a comprehensive examination of stoichiovariants YHO thin films produced by reactive e-beam evaporation. Comprising three distinguishable layers, each enriched with hydrogen and/or oxygen, these structures exhibit localized stoichiometric variations.

We provide insights into the intricate chemical bonding within YHO, the local environment surrounding yttrium atoms, a substantial disorder in the first yttrium coordination shell, and a less pronounced splitting in the second shell containing 12 yttrium atoms compared to the oxide thin film. We also reveal a cation charge state of approximately +2.5 and offer data on the refractive index and extinction coefficient for both transparent and dark states within the photon energy range from 0 to 6 eV.

2 Experimental

The thin film samples were produced using the e-beam evaporator attached to the SIDRABE SAF25/50 multi-functional vacuum cluster tool (kept at a high vacuum level of ~6.00×10^{-5} Pa during the entire procedure) and operated in the ISO 8 class clean room environment. The evaporation chamber was baked out for 72 h at 368 K (±5 K). The substrates were loaded and unloaded to/from the system using the robotic arm through a load lock without breaking the process/evaporation chamber vacuum. Prior to the deposition the substrates were successively cleaned in the ultrasonic bath with acetone, isopropanol, and deionized water (15 min each) and were then dried by blowing N_2 gas. The substrates were positioned in a parallel orientation, 26 cm away from the crucible. The base pressure of the evaporation chamber was taken down to 3.00×10^{-5} Pa. The evaporations of metallic yttrium (sample ***eb***$_3$), oxidized yttrium hydride (sample ***eb***$_4$), and yttrium oxide (sample ***eb***$_5$) thin films of around 200 nm in thickness, were carried out from Y pieces (%99.99, Purity) at 298 K (±5 K) in the presence of oxygen or mixed hydrogen and Ar (%35 H_2 + %65 Ar) atmosphere (for reactive evaporation) and without intentionally introducing reactive gas (for metallic thin film evaporation) onto the Si (001), soda-lime glass, and kapton substrates (detailed evaporation conditions can be found in Table 1). The substrates were rotated at 10 rpm during evaporation. The produced thin films were directly conveyed to the storage chamber (vacuum level, ~6.00×10^{-5} Pa). The samples were natively post-oxidized in the cluster tool, in which the vacuum pumps were turned off and the level of pressure was gradually (and naturally) increased (oxidation time ~ 72 h). No post-process was applied to the thin films.

Table 1: Evaporation conditions of the produced samples: the fabrication of the samples was carried out ***eb***$_3$, ***eb***$_4$ and ***eb***$_5$ respectively.

Sample	***eb***$_3$	***eb***$_4$	***eb***$_5$
Evaporated material/crucible	Y/W	Y/W	Y/W
Evaporation/substrate temperature (K)	~298	~298	~298
Reactant gas	–	%35H_2 + %65Ar	O_2
Base pressure (Pa)	~2.00e-05	~2.00e-05	~2.00e-05
Evaporation pressure (Pa)	~4.00e-05	~1.20e-03	~1.60e-04
Current (mA)	~34	~37	~37
Evaporation rate (A/s)	~0.8	~0.8	~0.8
Thickness (nm)	~200	~200	~200

The structure of thin films was investigated using the RIGAKU MiniFlex 600 benchtop X-ray diffractometer equipped with a CuK_α X-ray source. The measurements were conducted in the range of $2\theta = 5–60°$ with a step size of $\Delta 2\theta = 0.005°$, employing the Bragg-Brentano $\theta–2\theta$ diffraction geometry. For further structural analyses, a combination of transmission electron microscopy (TEM) and scanning electron microscopy (SEM) techniques was employed. The high-resolution SEM-FIB system, Helios 5 UX (Thermo Scientific), operating at 2 kV with the Through-the-lens detector (TLD), was utilized for lamella preparation. To prepare lamella samples, a sputter-coating process was performed using a 30 nm thick gold layer, followed by the deposition of a Pt layer (thicker than the gold layer) using Focused Ion Beam (FIB) to protect the surface from ion beam damage. The resulting lamellas were then analyzed using a transmission electron microscope (TEM, Tecnai G20, FEI) operating at 200 kV.

The chemical state analyses have been conducted using X-ray photoelectron spectroscopy (Escalab 250XI, ThermoFisher). The pressure in the system, with the charge neutralizer activated during spectrum acquisition, was maintained below 10^{-5} Pa thanks to rotary and turbomolecular pumps. The samples were introduced into the XPS chamber under laboratory conditions (~300 K, 1.013×10^5 Pa or 1 atm). Prior to the measurements, the samples underwent sputter-etching to collect depth profile data. This process was accomplished using an Ar^+ gun with an ion energy of 2.0 keV for 5 s. The etched area measured 2×2 mm^2, and the incidence angle was set at 30° relative to the surface normal. The size of the analyzed sample area was 650×100 μm^2. We employed monochromated AlKα radiation ($h\nu = 1486.60$ eV) as the excitation source, utilizing a water-cooled anode operating at 150 W. To calibrate the binding energy, we performed adjustments relative to the adventitious carbon (C1s) at 284.8 eV for the corresponding samples, resulting in the shifting of all the spectra accordingly.

The sample $\boldsymbol{eb}_4$ has been characterized with time-of-flight energy elastic recoil detection analysis (ToF-E ERDA) and Rutherford Backscattering Spectrometry (RBS) to obtain the elemental concentration of chemical elements and their depth distributions. Both measurements were conducted at the 5 MV NEC Pelletron Accelerator at the Tandem Laboratory, Uppsala University [18]. ToF-E ERDA experiments have been performed with a beam of 36 MeV 127I+8 primary ions incident at 67.5° to the surface normal and a recoil detection angle of 45°. The ToF-E ERDA detector is a combined segmented anode gas ionization chamber and time-of-flight detector consists of a time-of-flight telescope followed by a gas ionization chamber detector, thus both energy and time-of-flight of recoiled particles are recorded working in a coincidence mode [19]. The depth profiles were derived from ToF-E spectra using the software Potku [20]. RBS measurements were conducted using 2 MeV He^+ primary ions, and backscattered particles were detected by a silicon surface barrier detector located at 170° concerning the incident beam. To avoid potential channeling effects in the single crystalline Si substrate samples were tilted 5° towards the detector and wiggled during the measurement. Recorded RBS spectra were analyzed and fitted employing SIMNRA [21]. Additionally, characteristic X-ray lines, produced under He^+ bombardment and collected by a silicon drift detector, were used for the identification of heavy impurities.

Optical properties of the film were obtained by means of spectroscopic ellipsometer (SE) WOOLLAM RC2 in the spectral range from 210 to 1690 nm (5.9–0.7 eV). The main ellipsometric angles were measured at the incident angles of (55–70)° with the 5°-step. Refractive index n and extinction coefficient k dispersion curves were modeled using the Drude (DO), Gaussian (GO), and Herzinger-Johs parameterized semiconductor (HJPS) oscillator functions [22]. The optical properties of the Si/native SiO_2 and glass substrates were obtained from SE measurements to clean substrates without the films. In addition to standard reflection ellipsometry measurements for the $\boldsymbol{eb}_4$ on Si substrate, $\boldsymbol{eb}_4$ on glass were also studied to perform transmission measurements to increase precision for fundamental band gap E_g evaluation and to perform photochromic effect test. The surface roughness was modeled utilizing the Bruggeman effective medium approximation (EMA) [23]. The optical gradient of n and k was calculated by dividing the film layer into sub-layers with smaller thicknesses, and by applying the EMA considering the films as a mixture of voids and oxide in the case of the Y_2O_3 sample (***eb***$_5$) and as a mixture of YHO, Y_2O_3, and Y in case of YHO sample (***eb***$_4$) to vary the n and k values from the bottom to the top of the film [24]. The EMA mixture as YHO, Y_2O_3, and Y was chosen based on XPS results which provided information on 3-layer structure of ***eb***$_4$ film with the presence of interface layers with different distributions of Y binding energies. The (n; k) dispersion curves obtained for the ***eb***$_3$ (Y) and ***eb***$_5$ (Y_2O_3) samples were used to model the graded EMA optical properties of ***eb***$_4$ and optical properties of YHO: based on that, established YHO (n; k) dispersion curves for ***eb***$_4$ are approximative. The E_g for directly allowed transition is obtained as a fitting parameter from HJPS for ***eb***$_4$ and ***eb***$_5$. The mean square error (MSE) between modeled and experimental SE data was obtained in the range of 2–80. High MSE was obtained for ***eb***$_4$ sample due to its inhomogeneity. SE experimental data model-based regression analyses were performed by the Woollam software CompleteEASE®.

X-ray absorption spectra of thin films ***eb***$_3$, ***eb***$_4$, and ***eb***$_5$ were obtained on Kapton substrates. All samples were individually packed in an Ar atmosphere glove box using aluminum envelopes. For sample ***eb***$_3$, (metallic thin film), measurements were taken through the Al packing, while for samples ***eb***$_4$ (oxidized yttrium hydride thin film) and ***eb***$_5$ (fully oxidized yttrium oxide thin film), measurements were performed shortly after unpacking. The spectra were recorded at the Y K-edge (17,038 eV) in fluorescence mode at the DESY PETRA III P65 undulator beamline [25]. The harmonic rejection was achieved by an Rh-coated silicon plane mirror. A fixed exit Si (111) double-crystal monochromator was used. The X-ray intensity before the sample was measured by an ionization chamber filled with a mixture of N_2 and Ar gasses. The fluorescence signal from the sample was recorded with a passivated implanted planar silicon (PIPS) detector placed at 90° to the incident beam. X-ray absorption spectra of three reference samples (yttrium foil, bulk cubic yttrium oxide (c-Y_2O_3) powder, and yttrium oxyhydride (YHO) powder) was additionally recorded in transmission mode. The X-ray absorption near-edge structure (XANES) and extended X-ray absorption fine structure (EXAFS) spectra were extracted from the experimental X-ray absorption spectra using the XAESA code [26].

3 Results and discussion

The X-ray diffraction patterns of the samples are presented in Figure 1, with comparisons made to the standard JCPDS database for cubic (α-phase, PDF Card 01-089-5592) and monoclinic (β-phase, PDF Card 00-044-0399) yttria (Y_2O_3), cubic yttrium hydride ($YH_{1.98}$, PDF Card 04-002-6938), and hexagonal close-packed yttrium (Y, PDF Card 00-033-1458) and yttrium hydroxide ($Y(OH)_3$, PDF Card 01-083-2042). Furthermore, in this context, we referred to a prior investigation conducted by Sørby et al. regarding high-contrast yttrium-based photochromic oxyhydride powder [11].

The sample ***eb***$_3$ appears to be predominantly composed of the monoclinic phase (the main peak(s) detected at around $2\theta = 31°$ might correspond to (002) of α-Y and/or (401), (40-2) of β-yttria planes). This could be attributed to the oxidation of yttrium during or after evaporation (which will be supported by XPS analyses). A previous study conducted by Arslan et al. suggests that even at very low oxygen partial

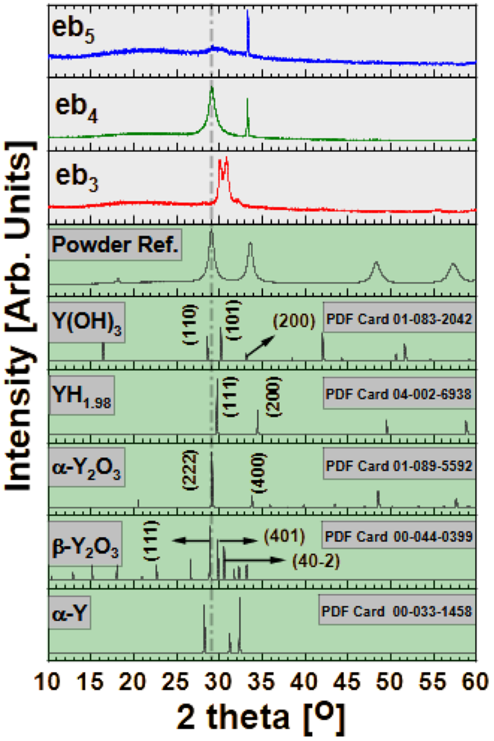

Figure 1: XRD pattern of the samples ***eb***$_3$, ***eb***$_4$ and ***eb***$_5$ with the ICDD reference diffractograms of α-phase Y (hcp), Y_2O_3 (cubic), β-phase Y_2O_3 (monoclinic), $YH_{1.98}$ (cubic), and $Y(OH)_3$ (hcp). In addition to that, the diffractogram that belongs to high-contrast yttrium-based oxyhydride photochromic powder was used as a reference [11].

pressure levels (~10^{-6} Pa), the metallic yttrium phase coexists with yttria [27]. Conversely, the sample ***eb***$_5$, which is fully oxidized, exhibits either amorphous or nano-crystalline structure/diffraction pattern (please take note of XAS part for comprehensive details regarding the supporting information on structure), as indicated by the blue line in the same figure. Due to the unclear position of hydrogen in the lattice and its effect on the crystal structure, we choose to reference fully oxidized yttrium structures that are relatively stable. The sample ***eb***$_4$ exhibited a single peak at approximately 29° (2θ). This peak's presence suggests that there might be simultaneous formation of cubic ([222] of α-yttria) and monoclinic ([111] of β-yttria) phases, and/or cubic ([111] of $YH_{1.98}$) phases. Alternatively, it could indicate the sole formation of the cubic phase. XAS analyses will provide more detailed information on the local structure of the sample ***eb***$_4$.

Additional analyses were conducted using electron microscopy to specifically enhance the reader's understanding of spectroscopic ellipsometry, ion-beam analysis, and X-ray photoelectron spectroscopy (which will be addressed below). These analyses aimed to investigate the sample ***eb***$_4$, which represents the photochromic property. The results of transmission electron microscopy (TEM) depict the morphology of the cross-section of the sample ***eb***$_4$, revealing the occurrence of a formation consisting of multiple layers (Figure 2).

This distinctive formation is observable in both lamellas extracted from films on different substrates: Si (Figure 2a) and soda-lime glass (Figure 2b). In both cases, the middle layer has a consistent thickness of ~85 nm. However, there is a noticeable difference of approximately 20 nm in the thicknesses of the top and bottom layers, on different substrates.

It is worth noting that the thickness of the surface oxide layer reported by Mongstad et al. [28] was around 8 nm, while in this study, the upper layer (likely oxide based on XPS and SE results, which will be discussed in subsequent sections) has a thickness of approximately 30 nm on a Si substrate and 50 nm on a glass substrate. Furthermore, a previous study conducted by Komatsu et al. revealed the formation of a bi-layer type yttrium oxyhydride thin film [6]. Whilst this particular batch of the film represents challenges in analyzing optical data (i.e. n and k), it provides significant insights into the dynamic formation of the cation's chemical state and potential chemical bonding scenarios involving Y, O, and H. The formation of this unusual multiple layer, which has not been previously reported in the literature, does not have a clear explanation. However, the formation likely occurred during the evaporation process and/or as a result of oxidation step.

In the context of this research, we employed photochromic YHO powder prepared via magnetron sputtering as a reference material for various techniques, including TEM.

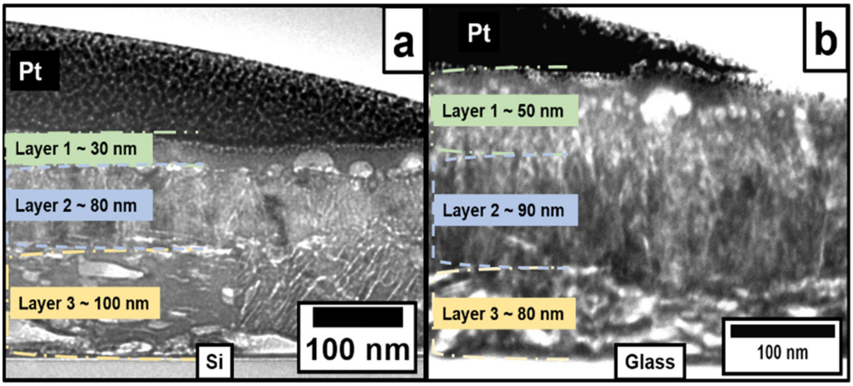

Figure 2: TEM image of the extracted lamellas from the sample ***eb***$_4$ (oxidized hydride, thin film): layered structure on Si substrate (a), layered structure on the soda-lime glass substrate (b). The thickness of the individual layers represents consistency on both substrates. Note that the samples were Pt-coated during the lamella preparation procedure.

Films produced via this method showcased distinct columnar domains/grains, as visually depicted in Figure S1 (Supplementary Figure). Additional comprehensive details about this specific sample can be found in another source [11]. A prior study acknowledged the likelihood of this formation promoting oxidation, which could potentially occur uniformly throughout its entire depth [29].

Nevertheless, the precise mechanism driving the formation of specific grain types remains uncertain at this juncture. Our observations using transmission electron microscopy unveil the intricate nature of this grain formation process. This mechanism may be associated with the formation of grains enriched with hydrogen and/or oxygen.

The depth-resolved chemical state identification of yttrium (Y3d) in the three samples (***eb***$_3$, ***eb***$_4$, and ***eb***$_5$) and oxygen (O1s) in the sample ***eb***$_4$ was performed using XPS. To gain insights into the spectroscopic behavior of the photochromic oxidized yttrium hydride thin film, two references were utilized in the form of metallic yttrium thin film (***eb***$_3$) and fully oxidized yttrium thin film (***eb***$_5$). Figure 3 shows both the thermodynamic stability of yttria and the oxygen affinity of yttrium metal. Additionally, Figure 3 reveals the simultaneous formation of yttrium in different chemical states within the oxidized yttrium hydride thin film, as evidenced by the variations in Y3d binding energy. Figure 3.a3 and .b3 depict the depth-resolved Y3d spectrum of sample ***eb***$_3$ in 3D and 2D respectively. The peak around 155.80 eV suggests the presence of Y^0 ($Y3d_{5/2}$). This observation aligns with the results reported in a previous study [30]. Furthermore, the peak observed at a position of 157.9 eV in the same spectrum (Figure 3.b3) likely corresponds to the formation of an oxide or hydride [31, 32]. Additionally, Figure 3.c3 provides insight into the oxygen content in the sample, which may result from the oxidation occurring during or after the growth process. Previous research conducted by Arslan et al. [27] supports the tendency of yttrium to form oxides, even at very low ($\sim 10^{-6}$ Pa) oxygen partial pressure levels.

Figure 3.a5 and .b5 illustrate the depth-resolved X-ray photoelectron spectrum of the sample ***eb***$_5$ in 3D and 2D, respectively. The presence of a peak observed at approximately 157 eV suggests the complete oxidation of yttrium, indicating the formation of yttrium oxide (Y_2O_3) [32]. The minor peak observed at approximately 155.30 eV is likely a result of Ar^+ etching and the formation of various oxidation states, potentially including (Y^0) [33]. Moreover, Figure 3.c5 reveals the atomic concentration ratio between yttrium and oxygen, providing evidence that the predominant phase in the sample is Y_2O_3.

In Figure 3.x4y (x: a,b,c; y: -a,b) the spectroscopic information that belongs to ***eb***$_4$ is given. The three layers' formation of the oxidized yttrium hydride thin film can

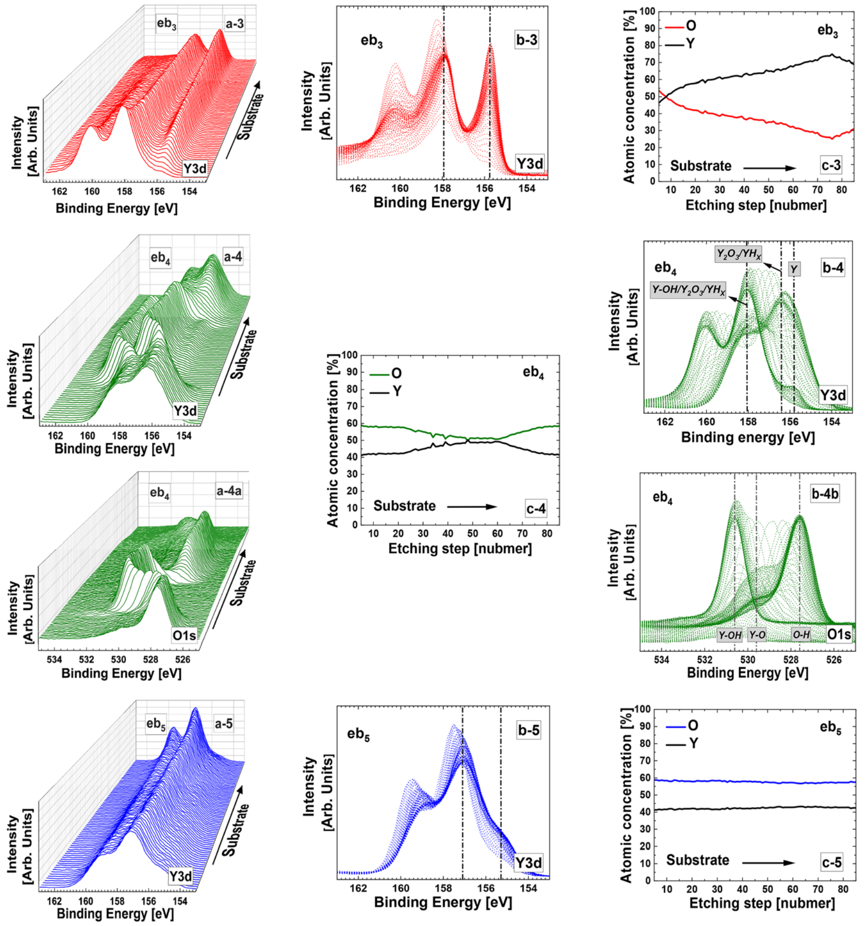

Figure 3: XPS depth profile of samples: ***eb***$_3$ (metallic): (a-3)-depth-resolved Y3d spectrum dynamic in 3D, (b-3)-corresponding Y3d binding energy representation/density mapping of the spectrum in Figure 3a-3 in 2D, (c-3)-atomic concentration of yttrium and oxygen depending on depth. ***eb***$_4$ (oxidized hydride): (a-4)-depth-resolved Y3d spectrum dynamic in 3D, (b-4)-corresponding Y3d binding energy representation/density mapping of the spectrum in Figure 3a-4 in 2D, (c-4)-atomic concentration of yttrium and oxygen depending on depth; (a-4a)-depth-resolved O1s spectrum dynamic in 3D, (b-4b)-corresponding O1s binding energy representation/density mapping of the spectrum in Figure 3a-4a in 2D, ***eb***$_5$ (oxide): (a-5)-depth-resolved Y3d spectrum dynamic in 3D, (b-5)-corresponding Y3d binding energy representation/density mapping of the spectrum in Figure 3a-5 in 2D, (c-5)-atomic concentration of yttrium and oxygen depending on depth.

easily be recognized in the same figures (existing literature reports the formation of a surface oxide layer, which is commonly accepted as a two-layer structure [5, 28]). The depth-resolved spectrum of Y3d$_{5/2}$ in three dimensions is illustrated in Figure 3.a4. In this figure, the three layers are categorized into two distinct classes: interface layers and surface layers. Additionally, the corresponding two-dimensional spectrum is presented in Figure 3b4. The small peak detected at around 155.8 eV most likely indicates Y^0 formation [34]. In contrast, the primary peak observed at approximately 156.4 eV suggests the formation of Y_2O_3 and/or YH_x [31, 35]. Moreover, the peak detected at around 158 eV most likely indicates the simultaneous formation of Y_2O_3, YH_x or Y–OH, either individually or in combination, possibly in a double or triple fashion [31, 32, 36]. Figure 3.a4a presents the depth-resolved O1s spectrum in three dimensions. This spectrum reveals the presence of multiple layers, which was previously observed and reported in the TEM results. Moreover, the corresponding two-dimensional representation is given in Figure 3.b4b. The peaks observed at approximately 527, 529, and 530 eV may be attributed to the formation of O–H, Y_2O_3 and Y–OH respectively [36–38]. In general, the peaks detected at the spectrum represent fluctuation around some specific values during the depth profile investigation that can result from the interaction between Ar^+ and the sample. The effect of Ar^+ etching on the binding energy of the related element/oxidation state is a well-studied phenomenon [33].

Finally, Figure 3.c4 illustrates the variation in yttrium and oxygen concentration ratios with depth for the sample ***eb***$_4$. The results indicate a decreasing trend in oxygen concentration towards the intermediate layer, stabilizing at an approximate 1:1 (Y:O) ratio. From there, the oxygen concentration begins to increase towards the bottom of the thin film, eventually reaching a balanced ratio of 2:3 (Y:O). Nevertheless, further investigations employing an alternative method suggested by Greczynski, and Hultman [38] for binding energy calibration for different H/O-containing thin films must be performed to create an enhanced comprehension of chemical bondings between Y, H, and O ternary (some of the possible formations Y–H, Y–OH, H–Y–O) and their effect on XPS spectrum.

Additional composition analyses of the sample ***eb***$_4$ were performed to construct a better understanding of its formation/oxidation/hydrogenation dynamics. Ion beam-based techniques revealed that apart from the expected main constituents O, H, and Y, the film contains 1–2 at% of C as well as F at the promille level (Figure 4).

While the surface region (25–30 nm) features a nearly stoichiometric oxide, the concentration of O decreases slightly with depth featuring a minimum at the depth of 50–55 nm. This dip in oxygen concentration is also associated with an increase in H concentration (Figure 4a [and Figure 3-c4, XPS depth profile mapping]) and followed by an increase of O content near the interface. The disparities in the results obtained from XPS and IBA most likely arise from the measurement of slightly different locations (please notice Figure 2). The total thickness of the film is estimated to be approx. 250 nm, assuming a bulk density of 6.44×10^{22} at/cm^3 as it was demonstrated

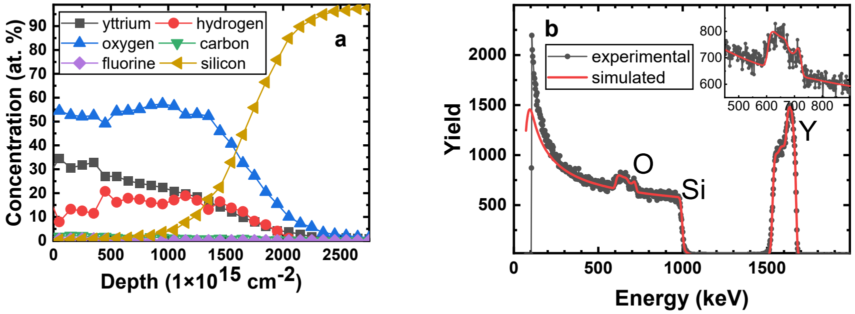

Figure 4: a-Depth profile of chemical elements in the sample ***eb***$_4$ derived from ToF-E ERDA. b-RBS spectrum (black dots) for the sample ***eb***$_4$ and corresponding fit (red line) done using SIMNRA.

in Ref. [4] for sputter deposited YHO films. Note that YHO films prepared by e$^-$-beam evaporation are shown to have lower density than those deposited by magnetron sputtering [7].

The measured and modeled spectroscopic ellipsometry data for all samples are presented in Figure 5 with respective MSE values. The complex refractive index dispersion curves (n; k) as a function of photon energy for all three samples are given in Figure 6. The thickness, n, k, surface roughness, and E_g values for all samples are summarized in Table 2. The values of n and k for the Y sample (***eb***$_3$) are lower compared to our previous results [27] (see Table 3).

The ***eb***$_4$ thin film on both substrates exhibits a significant optical gradient (Figure 7a). The parameters n and k increase starting from the thickness of ~60–100 nm up to ~175–220 nm and then they decrease towards the surface of the films. The high MSE for ***eb***$_4$ samples (Figure 5) is related to the complex inhomogeneities in YHO films,

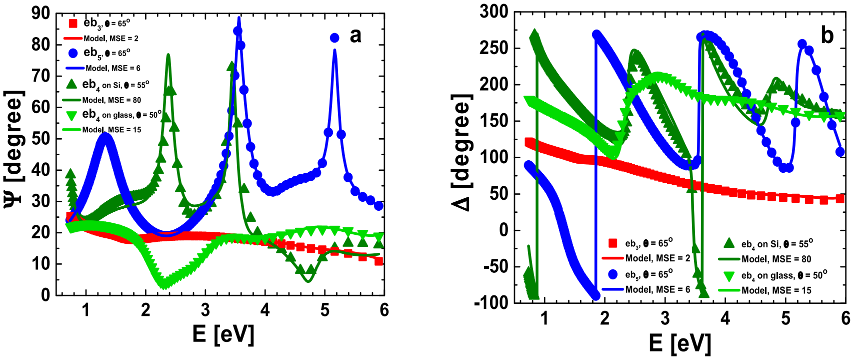

Figure 5: Main ellipsometric angles Ψ (a) and Δ (b) as a function of photon energy E for four samples at an incident angle the model fit is demonstrated as a continuous line with the respective MSE.

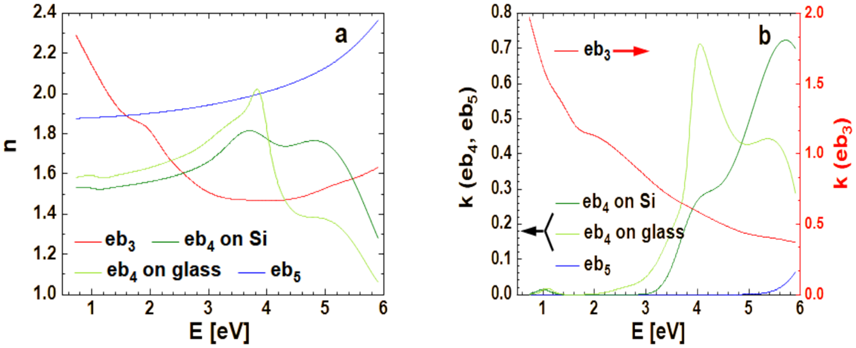

Figure 6: Refractive index *n* (a) and extinction coefficient *k* (b) as a function of photon energy *E* for four samples: ***eb***$_3$, ***eb***$_4$ on Si and glass substrates, and ***eb***$_5$ sample.

Table 2: Obtained values of the different films on Si: *d* – thickness of the films, S_r – surface roughness, E_g – optical band gap, *n,* and *k* at 550 nm, oscillators used to model complex dielectric function of the films.

Film		***d*, nm**	**S_r, nm**	**E_g, eV**	***n***	***k***	**Oscillators**
Y		200[a]	–	–	1.705 ± 0.001	1.077 ± 0.001	1 DO, 5 GO
YHO	Si	263 ± 52	7 ± 3	3.50 ± 0.20	1.58 ± 0.04	0	1 HJPS, 2 GO
	SiO_2	247 ± 22	7 ± 1	3.48 ± 0.05	1.66 ± 0.02	0.007 ± 0.001	1 HJPS, 3 GO
Y_2O_3		149.7 ± 0.1	5.54 ± 0.03	5.86 ± 0.42	1.910 ± 0.002	0	1 HJPS

[a]The film is not transparent for the given SE spectral range: the thickness is obtained with a profilometer.

Table 3: Refractive index at 550 nm and optical band gap for Y and Y_2O_3 thin films reported in the literature.

Description	**(*n; k*)@550 nm**	**E_g, eV**	**Ref.**
Metallic yttrium Y			
SiO_2 substrate/Y metal film/Y_2O_3 top layer deposited employing an ion beam sputtering	(~1.23; ~2.26)	–	[39]
200 nm Y film deposited by reactive pulsed direct current magnetron sputtering on Si[001] substrate	(1.53; 1.44)	–	[27]
200 nm thin film deposited by reactive e-beam evaporation on Si[001] substrate	(1.71; 1.08)	–	This work
Yttrium oxyhydride YHO			
460 nm YH_xO_y thin film deposited by reactive pulsed-DC magnetron sputtering on Si substrate	1.86@633 nm at 2.65 Pa sputtering pressure	2.79	[40]

Table 3: (continued)

Description		**(*n; k*)@550 nm**	**E_g, eV**	**Ref.**
60–1570 nm YHO thin films deposited by pulsed in-line dc magnetron sputtering machine on glass substrates; E_g dependence on grain size (~6–12 nm)		–	2.85–3.60	[4]
280 nm thin film deposited by reactive e-beam evaporation on a glass substrate		(1.66; 0.007)	3.48	This work
Yttrium oxide Y_2O_3				
400 nm thin film deposited by means of an ion beam sputtering on SiO_2 substrate		(~1.58, ~0)	–	[39]
Nanocrystalline thin films were grown by PVD on quartz substrates		1.79–1.90 (for substrate temperature during film deposition of 323–673 K)	–	[41]
Thin films were grown on unheated [100] Si wafers with 1.2–2 μm SiO_2 buffer layer	e-beam deposition	1.718 (process pressure 2.93×10^{-2} Pa with an O_2 flow rate of 70 cm)		[42]
		1.741 (8.00×10^{-3} Pa, 10 sccm)		
		1.917 (10.00×10^{-3} Pa, no O_2 flow)		
	IBAD[a]	1.911 (2.00×10^{-2} Pa, 25 sccm)		
	HiTUS[b]	1.660 (1.09×10^{0} Pa, 5 sccm)		
		1.868 (2.66×10^{-1} Pa, 9 sccm)		
Bulk cubic Y_2O_3		1.934		
Thin films on Si		~1.645 (973 K; ion beam, 4.00×10^{-3} Pa)		[43]
		~1.765 (973 K; IBAD, 150 eV O_2)		
		~1.895 (room temperature; ion beam)		
Thin films were grown by CVD on quartz and Si substrates		1.65–1.73	5.62–5.80	[44]
Thin films on [100] Si wafers and quartz substrates by radio-frequency magnetron sputtering		~1.70–1.94 (substrate temperature from room temperature to 773 K)	5.91–6.15	[45]
420 nm thin film deposited by reactive pulsed direct current magnetron sputtering on Si[001] substrate		(1.89; 0.01)	5.86	[27]
150 nm thin film deposited by reactive e-beam evaporation on Si[001] substrate		(1.91; 0)	5.86	This work

[a] IBAD – ion beam-assisted deposition. [b] HiTUS – reactive sputtering with oxygen in a standard high target utilization sputtering system.

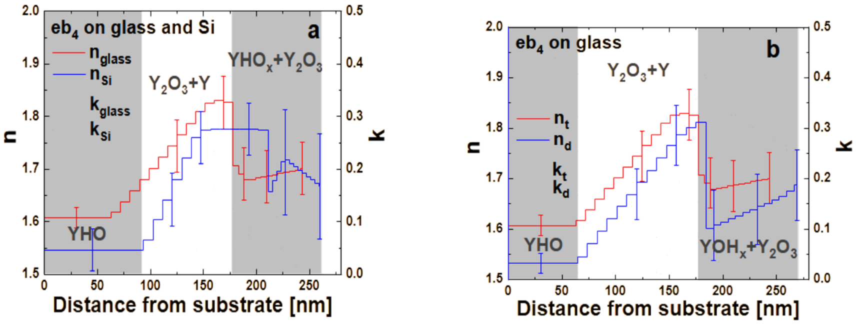

Figure 7: Depth profile of ***eb***$_4$ at 1.67 eV on (a) both substrates and for (b) transparent and dark state (sample on glass).

which could not be fully described by the graded EMA model [23] where these films are considered as a three-layer structure in correspondence with XPS results (Figure 3 [represented with green color]).

The illustrative image of the model fit is given in Figure 8. The 1st YHO layer has no gradient since no variation in Y and O content was found. The 2nd and the 3rd layers are considered with the optical gradient. Model 1 considers the top YHO layer as an EMA gradient with voids, and the middle layer has a gradient of EMA mixture of Y_2O_3 and Y. This model provided MSE larger than 100. Then this model was complemented with the presence of Y in the top and bottom layers which gave no improvement. Model 2 gave MSE around 80, where the top YHO layer is an EMA mixture with Y_2O_3, and the middle layer has a gradient of EMA mixture of YHO, Y_2O_3 and Y. Model 2 assumes that the dominant phase on ***eb***$_4$ is YHO, which is consistent with the XPS considerations.

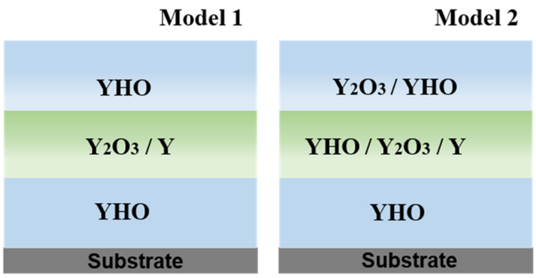

Figure 8: Illustrative image of graded EMA model for ***eb***$_4$ (oxidized hydride) sample. The 1st YHO layer has no gradient. The 2nd and the 3rd layers are considered with the optical gradient (illustrated as a gradient color fill). Model 1 consists of the top YHO layer as a gradient with voids and the middle layer as an EMA gradient of Y_2O_3 and Y. Model 2: the top YHO layer as EMA gradient with Y_2O_3, and the middle layer as EMA gradient of YHO, Y_2O_3 and Y.

The observed increase of (*n*; *k*) towards the middle of the ***eb***$_4$ sample (Figure 7a) is related to the increase of the EMA volume fraction of Y_2O_3 and Y since (*n*; *k*) of Y at 1.67 eV is higher concerning (*n*; *k*) of YHO. A significant increase in *k* around 150 nm and 200 nm film thickness for ***eb***$_4$ on glass and Si, respectively relates to a larger Y volume fraction. Also, XPS data suggest an interphase layer with most likely Y^0 formation (Figure 3), but near the bottom layer of the film. This could be explained by the effect of Ar^+ etching on the binding energy of the related element/oxidation state and/or measurements provided on the different places of the sample with different inhomogeneities. Nevertheless, the increase in Y and Y_2O_3 content towards the middle of the film obtained by SE is relatively consistent with XPS data presented in Figure 3. On the other hand, XPS shows a linear increase and decrease of Y and O content in YHO thin films (Figure 3). Unfortunately, the modeling of linear increase and decrease of (*n*; *k*) within the depth of the YHO thin films gave a very high MSE error. Probably this film contains some other inhomogeneity, which cannot be represented completely by this non-linear depth profile (Figure 7a). Other investigations should be provided to clarify this situation.

Photochromic effect of the sample ***eb***$_4$ was tested by SE. The SE measurements on ***eb***$_4$ sample on glass was realized in reflection and transmission modes before and after illumination of the sample with UV light. The complex dielectric functions (*n*; *k*) and experimental and modeled transmission spectra in transparent and dark states are illustrated in Figure 9. The increase of the extinction coefficient from ~3.5 eV up to IR is observed for the sample ***eb***$_4$ in the dark state for the given light source wavelength and power. The *k* increase is also observed in the depth profile of this sample (Figure 7b) suggesting significant structural changes in YHO thin film.

The gap energies E_{gap} for three peaks obtained in (*n*; *k*) dispersion curves (Figure 9), (*n*; *k*) values at 550 nm for transparent and dark states are summarized in

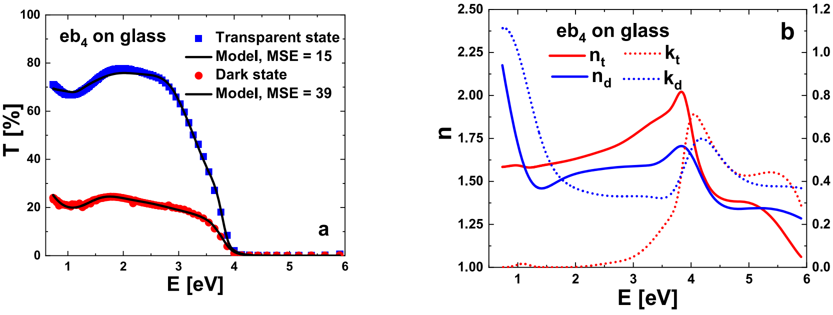

Figure 9: Measured and modeled transmission spectra (a) and corresponding complex refractive index dispersion curves (b) for ***eb***$_4$ sample on glass in a transparent and dark state.

Table 4. In the dark state, the refractive index decreases, the extinction coefficient increases, and the energy gaps for direct electron transition also decrease. The color of the film in the dark state was found to be dark brown. It was not possible to find any evidence in the literature about the optical properties of YHO thin film deposited by reactive e-beam evaporation. There are some references for YH_xO_y thin films in Table 3.

The values of n and k for the ***eb***$_3$ sample are lower with respect to our previous results [27] (Table 3). This can be explained by the sputtering conditions. This Y sample (***eb***$_3$) was sputtered at slightly lower sputtering pressure and lower gun current resulting in Y material with lower electrical conductivity due to Y oxidation. In the work of Santjojo et al. [39], where Y thin film was deposited utilizing an ion beam sputtering in the multilayer structure of $SiO_2/Y/Y_2O_3$, the k values are much higher with respect to this work. This is related to the fact that Y film was protected from oxidation since it was positioned between SiO_2 and Y_2O_3. Moreover, in our case Y film after deposition was kept in the air: as showed by XPS (Figure 3) the layer of the Y got oxidized resulting in the lower k values as evaluated by SE.

The sample ***eb***$_5$ has an optical gradient (Figure 10) due to the porosity: the n decreases from the bottom to the top of the film due to the increase of the EMA volume fraction of voids. The n and E_g values of the sample Y_2O_3 is comparable with our previous result [27] and with reports presented in the literature (see Table 3) except for the work of Santjojo et al. [39]: they reported lower n values of Y_2O_3 thin film, which can be related with the high porosity of the film.

The results we obtained from the aforementioned characterization methods demonstrate the formation of localized stoichiometric variants, enriched in either H or O. This finding hints at a potential alignment with and support for the outcomes of the research conducted by Hans et al. [14].

Table 4: The electron transition energies E_{gap}, n, and k at 550 nm for ***eb***$_4$ thin film on Si and glass substrates.

Substrate	**E_{gap}, eV**		**n**		**k**	
	Transparent	**Dark**	**Transparent**	**Dark**	**Transparent**	**Dark**
Si	3.50 ± 0.20 2.68 ± 0.39 0.56 ± 0.21	–	1.58 ± 0.04	–	0	–
SiO_2	3.48 ± 0.05 1.60 ± 0.40 0.41 ± 0.20	3.15 ± 0.29 1.16 ± 0.33 0.11 ± 0.10	1.66 ± 0.02	1.56 ± 0.04	0.007 ± 0.001	0.35 ± 0.02

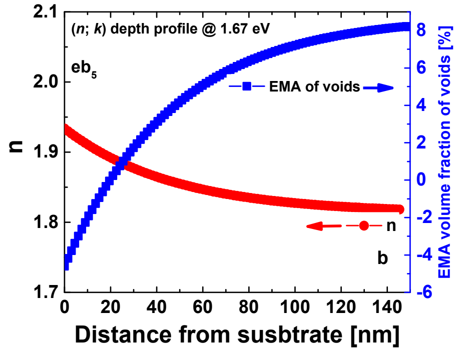

Figure 10: Depth profile of refractive index at 1.67 eV and EMA volume fraction of voids for ***eb***$_5$ sample.

The experimental Y K-edge XANES spectra and their first derivatives for three thin films (***eb***$_3$, ***eb***$_4$, and ***eb***$_5$) and three reference compounds (Y foil, bulk c-Y_2O_3, and YHO powder) are shown in Figure 11. The Y K-edge XANES spectra are dominated by the 1s(Y) → np(Y) dipole-allowed transitions. The position of the first maximum of the XANES derivative corresponds to the absorption edge and is located at 17,038 eV for the yttrium foil. In the metallic yttrium (***eb***$_3$) thin film the edge is slightly shifted to 17,039 eV indicating partial oxidation of the film. The position of the edge in yttrium oxide ***eb***$_5$ thin film and bulk c-Y_2O_3 is located at the energy of about 17,041 eV corresponding to the complete oxidation of yttrium ions. The position of the edge in YHO powder is at 17,040.5 eV, i.e. at 2.5 eV larger energy than in the yttrium foil but at 0.5 eV smaller energy than in bulk c-Y_2O_3, suggesting a yttrium oxidation state of about 2.5+. The shape of XANES and its first derivative in oxidized yttrium hydride thin film ***eb***$_4$ is close to that in yttrium oxyhydride powder.

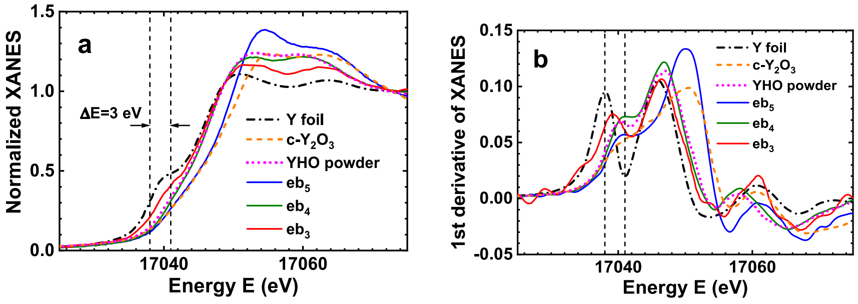

Figure 11: Normalized Y K-edge XANES spectra (a) and their first derivatives (b) for ***eb***$_3$, ***eb***$_4$, and ***eb***$_5$ thin films and three reference compounds (Y foil, bulk c-Y_2O_3, and YHO powder). Dashed vertical lines indicate the position of the absorption edge in the reference compounds.

The Y K-edge EXAFS spectra $\chi(k)k^2$ and their Fourier transforms (FTs) are shown in Figure 12. Note that the positions of peaks in FTs differ from the crystallographic values due to the phase shifts present in EXAFS. The EXAFS spectra and their FTs for yttrium foil and metallic yttrium thin film (***eb***$_3$) almost coincide.

The EXAFS spectra of yttrium oxide ***eb***$_5$ film and bulk c-Y_2O_3 show some similarity, however, all peaks in the FT of the film ***eb***$_5$ have reduced amplitudes suggesting the presence of disorder and nanocrystalline structure of the film [46, 47]. The EXAFS spectrum and its FT for oxidized yttrium hydride film ***eb***$_4$ are close to those for YHO powder.

More detailed information on the local environment in thin films was obtained from the analysis of the Y K-edge EXAFS spectra using reverse Monte Carlo (RMC) simulations with the evolutionary algorithm approach, which were performed by the EvAX code [48, 49]. We used the same approach as previously for the analysis of bulk c-Y_2O_3 [47].

The RMC simulation box was a cube with a size of $4a \times 4a \times 4a$ unit cells of YHO (where a = 5.323 Å [11]) with periodic boundary conditions. Note that the same box can be constructed from the $2a' \times 2a' \times 2a'$ unit cells of c-Y_2O_3 (where a' = 10.604 Å is the lattice parameter [50]). During the RMC simulations, the atoms in the box were randomly displaced till a good agreement between theoretical and experimental data in the wavelet space [51] was achieved (Figure 13).

The Morlet wavelet transforms of the EXAFS spectra were calculated in the k-space range of 4–10 Å^{-1} and the R-space range of 1.1–5.5 Å. The EXAFS spectra for each yttrium atom in the box were obtained within ab initio real-space multiple-scattering formalism using the FEFF8.5L code [52]. The simulations were repeated four times for each sample using different pseudorandom sequences of numbers to

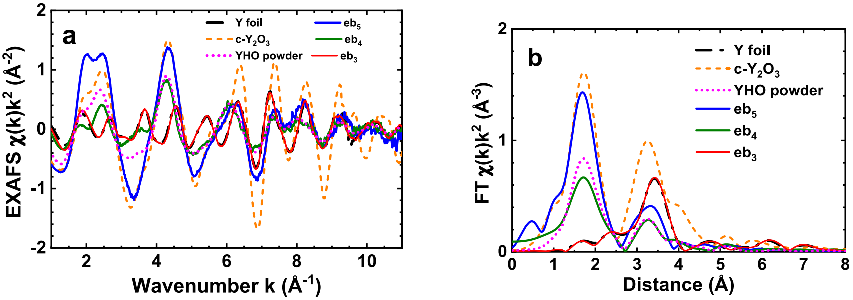

Figure 12: The Y K-edge EXAFS spectra $\chi(k)k^2$ (a) and their Fourier transforms (FTs) (b) for ***eb***$_3$, ***eb***$_4$, and ***eb***$_5$ thin films and three reference compounds (Y foil, bulk c-Y_2O_3, and YHO powder). Only the moduli of the FTs are shown.

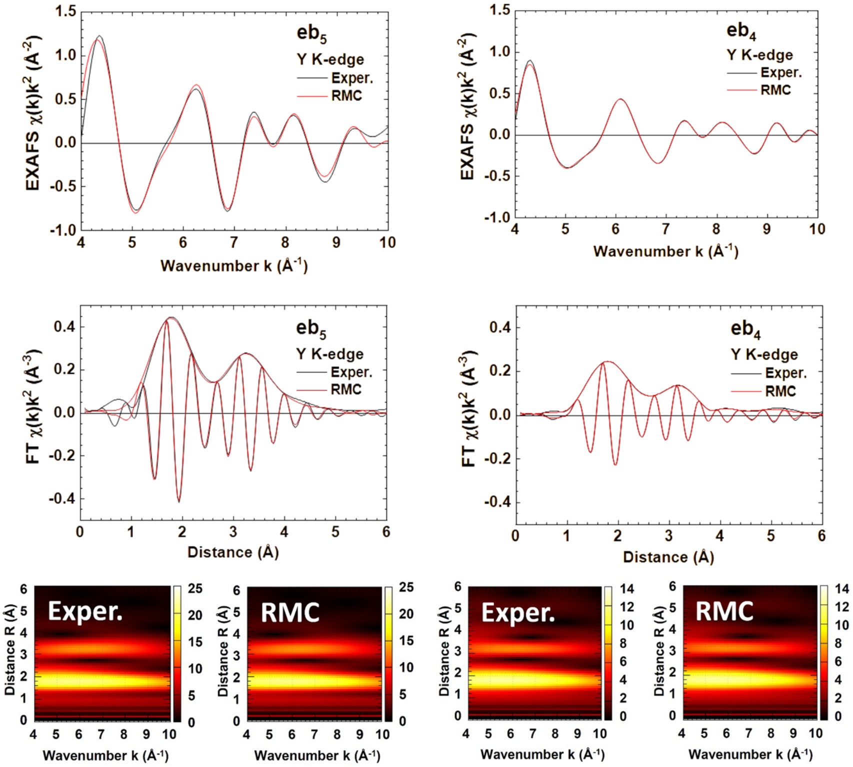

Figure 13: Experimental and RMC-calculated Y K-edge EXAFS spectra $\chi(k)k^2$ and their Fourier and Morlet wavelet transforms (FTs) for ***eb***$_5$ (left panels) and ***eb***$_4$ (right panels) thin films.

obtain reasonable statistics. The partial radial distribution functions (RDFs) Y–O and Y–Y were calculated from the coordinates of atoms in the simulation box and are reported in Figure 14.

In bulk c-Y_2O_3 having the space group *Ia*-3, there are two structurally non-equivalent yttrium atoms, which are located at the Wyckoff positions 8b (0.25, 0.25, 0.25) and 24d (u, 0, 0.25) (u = −0.0326 at T = 300 K [50]). Both yttrium atoms are octahedrally coordinated by oxygen atoms. At the same time, the second coordination shell of yttrium atoms is split into two groups of six yttrium atoms each at ~3.5 Å and ~4.0 Å. A similar situation was found in the Y–Y RDF obtained by the RMC for the thin film ***eb***$_5$. In the oxidized yttrium hydride thin film ***eb***$_4$, a larger disorder is present in the first coordination shell of yttrium leading to a decrease of the first peak in the Y–O RDF due to the broadening of the Y–O distribution (Figure 14). Moreover,

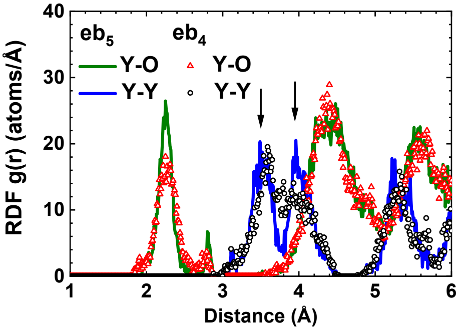

Figure 14: Partial radial distribution functions (RDFs) $g(r)$ Y–O and Y–Y for the ***eb***$_4$ (open symbols) and ***eb***$_5$ (solid lines) thin films obtained using the RMC method from the Y K-edge EXAFS spectra. Arrows indicate two groups of yttrium atoms in the second shell.

the splitting of the second shell Y–Y distribution in the range of 3–4.5 Å becomes less pronounced, and the distribution of the more distant group of yttrium atoms at 4 Å becomes more broadened.

Note that the presence of splitting of the Y–Y RDF contradicts the space group *Fm*-3*m* which was previously found for polycrystalline yttrium oxyhydride powder in [11] from diffraction experiments: in the cubic *Fm*-3*m* structure, 12 yttrium atoms are located at the same distance of 3.76 Å.

4 Conclusions

In the scope of this investigation, we conducted a comprehensive and systematic examination of stoichiovariants oxidized yttrium hydride thin films produced through reactive e-beam evaporation. The characterization of these thin films falls into two primary categories. In the first category, we employed Transmission Electron Microscopy (TEM), X-ray Photoelectron Spectroscopy (XPS), Ion Beam Analysis (IBA), and Spectroscopic Ellipsometry (SE) to thoroughly analyze the multi-layer structure of the films. This examination aimed to reveal depth-resolved elemental distribution and assess potential chemical bonding contributing to the formation of oxidized yttrium hydride, mainly. In contrast, the second category involved the application of X-ray Absorption Spectroscopy (XAS) and X-ray diffraction (XRD) to analyze the effective oxidation state of the cation within the structure, examine the local environment of yttrium, and explore potential scenarios for crystallographic formation.

One of the most significant findings of this study is the observation of a multilayered oxidized hydride thin film exhibiting photochromic properties. What sets this multilayer formation apart is its composition-comprising distinct, localized stoichiometric variants that are rich in hydrogen and/or oxygen. The evidence supporting this conclusion primarily stems from XPS, SE, TEM, and IBA. Additionally, cross-sectional TEM image, IBA, and XPS depth-resolved measurements have revealed the presence of an oxygen-rich surface layer with a thickness of approximately 40 nm. This finding aligns with previous research, as confirmed by ion beam analysis [5] and neutron reflectometry [28].

From ellipsometry measurements, we determined film thickness, surface roughness, optical band gap, and (n, k) dispersion curves in the broad photon energy range (5.9–0.7 eV). For the first time, the (n, k) dispersion curves for e-beam YHO thin films is reported in the transparent and in the dark states after UV irradiation. Notably, we report a significant difference in the refractive index/extinction coefficient between the bleached state and the photodarkened state.

Finally, the change in the position of the Y K-edge in XANES spectra suggests an effective oxidation state of 3+ for most yttrium ions in yttrium oxide (eb_5) thin film, whereas a smaller oxidation state of about 2.5+ was found for yttrium ions in the oxidized hydride (eb_4) thin film. The analysis of EXAFS spectra by the RMC method indicates the nanocrystalline structure of both films. The local environment around yttrium ions in the oxide (eb_5) thin film is close to that in bulk c-Y_2O_3. At the same time, the first coordination shell of yttrium in the oxidized hydride (eb_4) thin film is more disordered, and the splitting of the second shell of yttrium containing 12 yttrium atoms is less pronounced than in the oxide (eb_5) thin film.

Acknowledgments: We acknowledge DESY (Hamburg, Germany), a member of the Helmholtz Association HGF, for the provision of experimental facilities (XAS). Parts of this research were carried out at PETRA III and we would like to thank Dr. Edmund Welter for his assistance in using the P65 beamline. Beam time was allocated for proposal I-20230822 EC.

Research ethics: Each of the authors confirms that this manuscript has not been previously published and is not currently under consideration by any other journal. Furthermore, all of the authors have approved the contents of this paper and have agreed to Zeitschrift für Physikalische Chemie’s submission policies.

Author contributions: Halil Arslan: Conceptualization (equal); Investigation (equal); Formal analysis (equal); Writing – original draft (equal); Writing – review & editing (equal). Alexei Kuzmin: Conceptualization (equal); Investigation (equal); Formal analysis (equal); Writing – original draft (equal); Writing – review & editing (equal). Ilze Aulika: Investigation (equal); Formal analysis (equal); Writing – original draft (equal); Writing – review & editing (equal). Dmitrii

Moldarev: Investigation (equal); Formal analysis (equal); Writing – original draft (equal); Writing – review & editing (equal). Max Wolff: Conceptualization (equal); Investigation (equal); Formal analysis (equal); Writing – original draft (equal); Writing – review & editing (equal). Daniel Primetzhofer: Conceptualization (equal); Investigation (equal); Formal analysis (equal); Writing – original draft (equal); Writing – review & editing (equal). Inga Pudza: Investigation (equal); Writing – original draft (equal). Karlis Kundzins: Investigation (equal). Anatolijs Sarakovskis: Investigation (equal). Juris Purans: Funding acquisition (equal); Resources (equal). Smagul Zh Karazhanov: Conceptualization (equal); Funding acquisition (equal); Resources (equal); Supervision (lead); Writing – original draft (equal); Writing – review & editing (equal).

Competing interests: The authors state no conflict of interest.

Research funding: JP, IA, and SZK acknowledge SWEB project 101087367 funded by the HORIZON-WIDERA-2022-TALENTS-01-01. The research leading to this result has been supported by the RADIATE project under the Grant Agreement 824096 from the EU Research and Innovation programme HORIZON 2020. Support of experiments using the tandem accelerator at Uppsala University by the Swedish Research Council VR-RFI (grant# 2019_00191) is gratefully acknowledged. Dmitrii Moldarev acknowledges a postdoctoral fellowship by the foundation Olle Engkvist Byggmästare (grant# 207_0423).

Data availability: The data that support the findings of this study are available from the corresponding author upon reasonable request.

References

1. Mongstad T., Platzer-Björkman C., Maehlen J. P., Mooij L. P., Pivak Y., Dam B., Marstein E. S., Hauback B. C., Karazhanov S. Z. A new thin film photochromic material: oxygen-containing yttrium hydride. *Solar Energy Mater. Solar Cells* 2011, *95*, 3596–3599.
2. Maehlen J. P., Mongstad T. T., You C. C., Karazhanov S. Lattice contraction in photochromic yttrium hydride. *J. Alloys Compd.* 2013, *580*, S119–S121.
3. Moldarev D., Moro M. V., You C. C., Baba E. M., Karazhanov S. Z., Wolff M., Primetzhofer D. Yttrium oxyhydrides for photochromic applications: correlating composition and optical response. *Phys. Rev. Mater.* 2018, *2*, 115203.
4. Moldarev D., Wolff M., Baba E., Moro M., You C., Primetzhofer D., Karazhanov S. Photochromic properties of yttrium oxyhydride thin films: surface versus bulk effect. *Materialia* 2020, *11*, 100706.
5. Moldarev D., Primetzhofer D., You C. C., Karazhanov S. Z., Montero J., Martinsen F., Mongstad T., Marstein E. S., Wolff M. Composition of photochromic oxygen-containing yttrium hydride films. *Sol. Energy Mater. Sol. Cells* 2018, *177*, 66–69.
6. Komatsu Y., Shimizu R., Sato R., Wilde M., Nishio K., Katase T., Matsumura D., Saitoh H., Miyauchi M., Adelman J. R., McFadden R. M. L., Fujimoto D., Ticknor J. O., Stachura M., McKenzie I., Morris G. D., MacFarlane W. A., Sugiyama J., Fukutani K., Tsuneyuki S., Hitosugi T. Repeatable photoinduced

insulator-to-metal transition in yttrium oxyhydride epitaxial thin films. *Chem. Mater.* 2022, *34*, 3616–3623.

7. Kantre K., Moro M., Moldarev D., Wolff M., Primetzhofer D. Synthesis and in-situ characterization of photochromic yttrium oxyhydride grown by reactive e−-beam evaporation. *Scr. Mater.* 2020, *186*, 352–356.
8. Pitthan E., Cupak C., Fellinger M., Moro M., Kioumourtzoglou S., Moldarev D., Wolff M., Aumayr F., Primetzhofer D. In-situ, real-time investigation of the formation of oxygen-containing rare-earth hydrides by combining a quartz crystal microbalance and Ion beam analysis. *Materialia* 2023, *27*, 101675.
9. Zapp N., Auer H., Kohlmann H. YHO, an air-stable ionic hydride. *Inorg. Chem.* 2019, *58*, 14635–14641.
10. Yamashita H., Broux T., Kobayashi Y., Takeiri F., Ubukata H., Zhu T., Hayward M. A., Fujii K., Yashima M., Shitara K., Kuwabara A., Murakami T., Kageyama H. Chemical pressure-induced anion order–disorder transition in LnHO enabled by hydride size flexibility. *J. Am. Chem. Soc.* 2018, *140*, 11170–11173.
11. Sørby M. H., Martinsen F., Karazhanov S. Z., Hauback B. C., Marstein E. S. On the crystal chemistry of photochromic yttrium oxyhydride. *Energies* 2022, *15*, 1903.
12. Baba E. M., Montero J., Strugovshchikov E., Zayim E. Ö., Karazhanov S. Light-induced breathing in photochromic yttrium oxyhydrides. *Phys. Rev. Mater.* 2020, *4*, 025201.
13. Montero J., Martinsen F. A., García-Tecedor M., Karazhanov S. Z., Maestre D., Hauback B., Marstein E. S. Photochromic mechanism in oxygen-containing Yttrium hydride thin films: an optical perspective. *Phys. Rev. B* 2017, *95*, 201301.
14. Hans M., Tran T. T., Aðalsteinsson S. M., Moldarev D., Moro M. V., Wolff M., Primetzhofer D. Photochromic mechanism and dual-phase formation in oxygen-containing rare-earth hydride thin films. *Adv. Opt. Mater.* 2020, *8*, 2000822.
15. Moro M. V., Aðalsteinsson S. M., Moldarev D., Wolff M., Primetzhofer D. Photochromism in isotopically labeled oxygen-containing yttrium–hydride and deuteride thin-film systems. *Phys. Status Solidi Rapid Res. Lett.* 2022, *16*, 2100508.
16. Kumazoe H., Igarashi Y., Iesari F., Shimizu R., Komatsu Y., Hitosugi T., Matsumura D., Saitoh H., Iwamitsu K., Okajima T., Seno Y., Okada M., Akai I. Bayesian sparse modeling of extended X-ray absorption fine structure to determine interstitial oxygen positions in yttrium oxyhydride epitaxial thin film. *AIP Adv.* 2021, *11*, 125013-1–125013-5.
17. Banerjee S., Chaykina D., Stigter R., Colombi G., Eijt S. W. H., Dam B., de Wijs G. A., Kentgens A. P. M. Exploring multi-anion chemistry in yttrium oxyhydrides: solid-state NMR studies and DFT calculations. *J. Phys. Chem. C* 2023, *127*, 14303–14316.
18. Ström P., Primetzhofer D. Ion beam tools for nondestructive in-situ and in-operando composition analysis and modification of materials at the Tandem Laboratory in Uppsala. *J. Instrum.* 2022, *17*, P04011.
19. Ström P., Petersson P., Rubel M., Possnert G. A combined segmented anode gas ionization chamber and time-of-flight detector for heavy Ion elastic recoil detection analysis. *Rev. Sci. Instrum.* 2016, *87*, 103303.
20. Arstila K., Julin J., Laitinen M., Aalto J., Konu T., Kärkkäinen S., Rahkonen S., Raunio M., Itkonen J., Santanen J. P., Tuovinen T., Sajavaara T. Potku–new analysis software for heavy ion elastic recoil detection analysis. *Nucl. Instrum. Methods Phys. Res. B: Beam Interact. Mater. At.* 2014, *331*, 34–41.
21. Mayer M. Simulation of RBS, ERD and NRA spectra. *AIP Conf. Proc.* 1999, *475*, 541–546.
22. Ferlauto A., Ferreira G. M., Pearce J. M., Wronski C. R., Collins R. W., Deng X., Ganguly G. Analytical model for the optical functions of amorphous semiconductors from the near-infrared to ultraviolet: applications in thin film photovoltaics. *J. Appl. Phys.* 2002, *92*, 2424–2436.

23. Aspnes D. E., Theeten J., Hottier F. Investigation of effective-medium models of microscopic surface roughness by spectroscopic ellipsometry. *Phys. Rev. B* 1979, *20*, 3292.
24. Pettersson L. A., Hultman L., Arwin H. Porosity depth profiling of thin porous silicon layers by use of variable-angle spectroscopic ellipsometry: a porosity graded-layer model. *Appl. Opt.* 1998, *37*, 4130–4136.
25. Welter E., Chernikov R., Herrmann M., Nemausat R. A beamline for bulk sample X-ray absorption spectroscopy at the high brilliance storage ring PETRA III. *AIP Conf. Proc.* 2019, *2054*, 040002.
26. Kalinko A. *XAESA v.0.07*, 2023. https://gitlab.desy.de/aleksandr.kalinko/xaesa.
27. Arslan H., Aulika I., Sarakovskis A., Bikse L., Zubkins M., Azarov A., Gabrusenoks J., Purans J. Reactive pulsed direct current magnetron sputtering deposition of semiconducting yttrium oxide thin film in ultralow oxygen atmosphere: a spectroscopic and structural investigation of growth dynamics. *Vacuum* 2023, *211*, 111942.
28. Mongstad T., Platzer-Björkman C., Mæhlen J. P., Hauback B. C., Karazhanov S. Z., Cousin F. Surface oxide on thin films of yttrium hydride studied by neutron reflectometry. *Appl. Phys. Lett.* 2012, *100*, 191604.
29. Cornelius S., Colombi G., Nafezarefi F., Schreuders H., Heller R., Munnik F., Dam B. Oxyhydride nature of rare-earth-based photochromic thin films. *J. Phys. Chem. Lett.* 2019, *10*, 1342–1348.
30. Fujimori A., Schlapbach L. Electronic structure of yttrium hydride studied by X-ray photoemission spectroscopy. *J. Phys. C: Solid State Phys.* 1984, *17*, 341.
31. Majumdar D., Chatterjee D. X-ray photoelectron spectroscopic studies on yttria, zirconia, and yttria-stabilized zirconia. *J. Appl. Phys.* 1991, *70*, 988–992.
32. Uwamino Y., Ishizuka T., Yamatera H. X-ray photoelectron spectroscopy of rare-earth compounds. *J. Electron Spectrosc. Relat. Phenom.* 1984, *34*, 67–78.
33. Greczynski G., Hultman L. Towards reliable X-ray photoelectron spectroscopy: sputter-damage effects in transition metal borides, carbides, nitrides, and oxides. *Appl. Surf. Sci.* 2021, *542*, 148599.
34. Powell C. J. Recommended auger parameters for 42 elemental solids. *J. Electron Spectrosc. Relat. Phenom.* 2012, *185*, 1–3.
35. Baba Y., Sasaki T. A. Chemical states and thermal stability of hydrogen-implanted Ti and V studied by X-ray photoelectron spectroscopy. *J. Nucl. Mater.* 1985, *132*, 173–180.
36. Mai L., Boysen N., Subaşı E., Arcos T. D. L., Rogalla D., Grundmeier G., Bock C., Lu H. L., Devi A. Water assisted atomic layer deposition of yttrium oxide using tris (N, N′-diisopropyl-2-dimethylamido-guanidinato) yttrium (iii): process development, film characterization and functional properties. *RSC Adv.* 2018, *8*, 4987–4994.
37. Guo X., Sun Y.-Q., Cui K. Darkening of zirconia: a problem arising from oxygen sensors in practice. *Sens. Actuat. B Chem.* 1996, *31*, 139–145.
38. Greczynski G., Hultman L. X-ray photoelectron spectroscopy: towards reliable binding energy referencing. *Prog. Mater. Sci.* 2020, *107*, 100591.
39. Santjojo D. J., Aizawa T., Muraishi S. Ellipsometric characterization on multi-layered thin film systems during hydrogenation. *Mater. Trans.* 2007, *48*, 1380–1386.
40. Zubkins M., Aulika I., Strods E., Vibornijs V., Bikse L., Sarakovskis A., Chikvaidze G., Gabrusenoks J., Arslan H., Purans J. Optical properties of oxygen-containing yttrium hydride thin films during and after the deposition. *Vacuum* 2022, *203*, 111218.
41. Wiktorczyk T., Biegański P., Serafińczuk J. Optical properties of nanocrystalline Y_2O_3 thin films grown on quartz substrates by electron beam deposition. *Opt. Mater.* 2016, *59*, 150–156.
42. Pearce S. J., Parker G. J., Charlton M. D. B., Wilkinson J. S. Structural and optical properties of yttrium oxide thin films for planar waveguiding applications. *J. Vac. Sci. Technol. A Vac. Surf. Films* 2010, *28*, 1388–1392.

43. Gaboriaud R., Pailloux F., Guerin P., Paumier F. Yttrium oxide thin films, Y_2O_3, grown by ion beam sputtering on Si. *J. Phys. D: Appl. Phys.* 2000, *33*, 2884.
44. Liu L., Kawaharamura T., Sakamoto M., Nishi M., Dang G. T., Sato S. The quality improvement of yttrium oxide thin films grown at low temperature via the third-generation mist chemical vapor deposition using oxygen-supporting sources. *Phys. Status Solidi (b)* 2021, *25*, 2100105.
45. Mudavakkat V., Atuchin V., Kruchinin V., Kayani A., Ramana C. Structure, morphology and optical properties of nanocrystalline yttrium oxide (Y_2O_3) thin films. *Opt. Mater.* 2012, *34*, 893–900.
46. Ordás N., Gil E., Cintins A., de Castro V., Leguey T., Iturriza I., Purans J., Anspoks A., Kuzmin A., Kalinko A. The role of yttrium and titanium during the development of ODS ferritic steels obtained through the STARS route: TEM and XAS study. *J. Nucl. Mater.* 2018, *504*, 8–22.
47. Jonane I., Lazdins K., Timoshenko J., Kuzmin A., Purans J., Vladimirov P., Gräning T., Hoffmann J. Temperature-dependent EXAFS study of the local structure and lattice dynamics in cubic Y_2O_3. *J. Synchrotron Radiat.* 2016, *23*, 510–518.
48. Timoshenko J., Kuzmin A., Purans J. Reverse Monte Carlo modeling of thermal disorder in crystalline materials from EXAFS spectra. *Comput. Phys. Commun.* 2012, *183*, 1237–1245.
49. Timoshenko J., Kuzmin A., Purans J. EXAFS Study of hydrogen intercalation into ReO_3 using the evolutionary algorithm. *J. Phys.: Condens. Matter* 2014, *26*, 055401.
50. Bonnet M., Delapalme A., Fuess H. Redetermination of the scattering length of yttrium. *Acta Crystallogr. Sect. A Cryst. Phys. Diffract. Theor. Gen. Crystallogr.* 1975, *31*, 264–265.
51. Timoshenko J., Kuzmin A. Wavelet data analysis of EXAFS spectra. *Comput. Phys. Commun.* 2009, *180*, 920–925.
52. Ankudinov A. L., Ravel B., Rehr J. J., Conradson S. D. Real-space multiple-scattering calculation and interpretation of X-ray-absorption near-edge structure. *Phys. Rev. B* 1998, *58*, 7565.

Supplementary Material: This article contains supplementary material (https://doi.org/10.1515/zpch-2023-0507).